12th International Symposium on Turbulence and Shear Flow Phenomena (TSFP12)
Osaka, Japan (Online), July 19-22, 2022

RESTRICTED NONLINEAR SCALES OF TURBULENT SECONDARY FLOWS OVER SPANWISE HETEROGENEOUS ROUGHNESS

Benjamin A. Minnick
Dept. of Mechanical Eng.
Johns Hopkins University
3400 N. Charles St.
Baltimore, MD, 21218, USA
bminnic2@jhu.edu

Xiaowei Zhu
Atmospheric & Oceanography Science
Princeton University
300 Forrestal Rd.
Princeton, NJ, 08540, USA
xz18@princeton.edu

Dennice F. Gayme
Dept. of Mechanical Eng.
Johns Hopkins University
3400 N. Charles St.
Baltimore, MD, 21218, USA
dennice@jhu.edu

ABSTRACT

The natural scale separation in the restricted nonlinear (RNL) modelling approach is exploited to build upon recent studies, e.g., Wangsawijaya (2020), that have used scale separation to provide insight into mechanisms underlying secondary motions in turbulent flow over spanwise heterogeneous roughness. In the RNL decomposition the large-scale comprises the streamwise averaged mean and the small-scales are defined through a dynamical restriction that leads to computational tractability, while providing good agreement with salient flow features. In agreement with the experimental work, our results indicate that energy of the large-scales is amplified over the low roughness region due to the secondary flow. The small-scales are shown to play a dominant role in the Reynolds stresses responsible for generation of the secondary flow. Conditional averaging of the RNL mean field reveals stronger momentum pathways over low roughness regions experiencing downwash in instances that differ from the time-averaged trends. Further analysis of the large scale indicates that meandering of low speed streaks in the RNL flow is in response to secondary flow momentum mixing.

INTRODUCTION

Turbulent flow over spanwise heterogeneous roughness has long been of interest due to its relevance in a wide range of applications. Although the problem has been well studied, a full understanding of how these surfaces affect the structural properties of the turbulent boundary layer has yet to be realized. This understanding is complicated by the difficulty in extending common techniques to evaluate skin-friction drag predictions over homogeneous rough surfaces, such as the Moody diagram or Hama roughness function (Nikuradse & Nikuradse, 1933; Moody, 1944; Hama *et al.*, 1954) to heterogeneous rough surfaces. Even the assumption of outer-layer similarity that turbulent statistics for flow over rough walls are comparable to smooth-wall predictions (Townsend, 1980; Schultz & Flack, 2005; Flack *et al.*, 2007) does not apply.

Recent studies aimed at expanding the understanding of these flows have focused on how the topography affects flow structure. In an early investigation along these lines, Barros & Christensen (2014) identify time-averaged alternating low- and high-momentum pathways (LMPs and HMPs respectively) flanked by streamwise vortices over a turbine blade eroded by foreign materials. This finding inspired others to study flow over topographies with sharp interfaces between high and low roughness regions (Willingham *et al.*, 2014; Anderson, 2015; Bai *et al.*, 2018; Chung *et al.*, 2018). This body of work classified the non-zero time-averaged streamwise vorticity as the second kind of Prandtl's secondary flow (Prandtl, 1952). This secondary flow is generated from spanwise variations in the Reynolds stresses and as a result induces transverse mixing that modifies momentum transfer in the boundary layer. These structures also lead to a secondary outer-layer peak in the streamwise energy spectra (Wangsawijaya, 2020).

Unsteady behavior of the momentum pathways and secondary flow was historically masked by time-averaging of data. However, analysis using correlations and conditional averaging of an experimental study of flow over herringbone riblets, uncovered meandering of the low-speed streaks (Kevin, 2017). Subsequent work has attributed this meandering to a streak-vortex instability described in Jeong *et al.* (1997), and later observed in the outer-layer at larger scales (Kevin *et al.*, 2019). There is also evidence that these large-scale streaks modulate small-scales near the wall (Awasthi & Anderson, 2018). This modulation is stronger in the LMP, as is the meandering.

Spanwise heterogeneous rough surfaces which effectively "lock" coherent streaks and rolls in a spanwise location and may provide insight regarding smooth-wall boundary layers, where such structures exist but are permitted to move freely. A reduced-order model shown useful in the study of such coherent structures is the restricted nonlinear (RNL) model, see e.g. Farrell *et al.* (2017); Gayme & Minnick (2019). The RNL representation decomposes the flow into a streamwise averaged mean component that is permitted to interact nonlinearly and perturbations whose nonlinear interactions are limited to those contributing to the mean. RNL turbulence is self-sustaining despite its reduced streamwise varying perturbation field (Thomas *et al.*, 2014). The model also reproduces accurate turbulent statistics at moderate Reynolds numbers when the perturbation field is restricted to wavelengths that coincide with the outer-layer surrogate dissipation spectra (Minnick & Gayme, 2019).

In this work, we employ the RNL large eddy simulation (RNL-LES) model introduced in Bretheim *et al.* (2018) to study turbulent flow over spanwise heterogeneous strip roughness. First we demonstrate that this reduced-order model predicts time-averaged secondary flow and momentum pathway trends consistent with observations in the literature. We then use the RNL decomposition to assess the contributions of the large-scale mean and small-scale perturbation field to the mixing and momentum transfer mechanisms in these flows. Our RNL analysis approach enables us to also examine the dynamics of the structures, which is carried out using a conditional averaging approach similar to that in Kevin (2017). The results uncover similar meandering behavior, which suggests momentum mixing is primarily due to the secondary flow.

THE RNL-LES MODEL

We take (x, y, z) to denote the streamwise, wall-normal, and spanwise spatial coordinates with respective domain extents (L_x, L_y, L_z). t denotes the temporal coordinate. The total filtered velocity field, $\tilde{\mathbf{u}}_{\mathrm{T}}(x,y,z,t)$, is decomposed into a mean component, $\tilde{\mathbf{U}}(y,z,t) = \langle \tilde{\mathbf{u}}_T \rangle_x$, where the angle brackets with the subscript x indicate streamwise averaging, and a streamwise perturbation component, $\tilde{\mathbf{u}}(x,y,z,t)$. The governing equations consist of divergence free conditions, $\nabla \cdot \tilde{\mathbf{U}} = \nabla \cdot \tilde{\mathbf{u}} = 0$, and momentum equations,

$$\partial_t \tilde{\mathbf{U}} + \tilde{\mathbf{U}} \cdot \nabla \tilde{\mathbf{U}} + \nabla \tilde{P} + \nabla \cdot \langle \tau \rangle_x = -\langle \tilde{\mathbf{u}} \cdot \nabla \tilde{\mathbf{u}} \rangle_x,$$
$$\partial_t \tilde{\mathbf{u}} + \tilde{\mathbf{U}} \cdot \nabla \tilde{\mathbf{u}} + \nabla \tilde{p} + \nabla \cdot (\tau - \langle \tau \rangle_x) = -\tilde{\mathbf{u}} \cdot \nabla \tilde{\mathbf{U}},$$

which are derived from the filtered Navier-Stokes equations with nonlinear interactions between perturbations are omitted (except those contributing to the mean), i.e., $\langle \tilde{\mathbf{u}} \cdot \nabla \tilde{\mathbf{u}} \rangle_x - \tilde{\mathbf{u}} \cdot \nabla \tilde{\mathbf{u}} = 0$. This dynamical restriction achieves the order-reduction wherein the modelled streamwise wavelengths are isolated and only interact with the streamwise constant mean.

The sub-grid scale stress tensor is modelled using the standard Smagorinsky model (Smagorinsky, 1963) with an eddy viscosity formulation for the deviatoric component of this tensor

$$\tau - \frac{1}{3}\mathrm{tr}(\tau) I = -2\nu_e \tilde{\mathbf{S}}_{\mathrm{T}}.$$

Since the RNL methodology clearly defines streamwise scales in terms of large-scales represented by the streamwise averaged mean and small-scales as the streamwise varying perturbations, subgrid-scales in the cross-plane are modelled using the mean component. The eddy viscosity is therefore taken to be using the product of the streamwise averaged filtered strain rate tensor,

$$\nu_e(y,z,t) = (C_s \Delta)^2 \sqrt{2 \langle \tilde{\mathbf{S}}_{\mathrm{T}} \rangle_x : \langle \tilde{\mathbf{S}}_{\mathrm{T}} \rangle_x}.$$

Mason wall-damping is used for the Smagorinsky coefficient,

$$C_s \Delta = \left[\left(\frac{1}{C_0 \Delta} \right)^n + \left(\frac{1}{\kappa (y + y_0(z))} \right)^n \right]^{-1/n},$$

with $n = 2$, von Kármán constant, $\kappa = 0.4$, and a spanwise varying roughness height y_0 to prescribe the spanwise heterogeneous roughness. The filter size is taken to be, $\Delta = (\Delta y \Delta z)^{1/2}$, instead of the traditional $\Delta = (\Delta x \Delta y \Delta z)^{1/3}$, and therefore we use a slightly higher constant of $C_0 = 0.23$ rather than the common value of $C_0 = 0.16$ (Bretheim *et al.*, 2018).

The spanwise heterogeneous roughness on the bottom boundary $(y = 0)$ is modelled using the equilibrium wall-model, following previous LES studies of spanwise heterogeneous roughness (Willingham *et al.*, 2014; Anderson, 2015). The streamwise $(i = 1)$ and spanwise $(i = 3)$ components of the total wall-stress are prescribed as,

$$\tau^{(w)}_{i,2}(x,z,t) = -u_*^2 \frac{\tilde{u}_{T,i}(x, y_1, z)}{|\mathbf{u}|},$$

where y_1 is the first grid point from the wall,

$$u_*(z) = \frac{|\mathbf{u}|}{\log(y_1/y_0(z))}, \quad \text{and} \quad |\mathbf{u}|(z) = \sqrt{\tilde{U}_1^2(y_1,z) + \tilde{U}_3^2(y_1,z)}.$$

This equilibrium wall-model differs from the traditional wall-model used in LES in that $|\mathbf{u}|$ is the magnitude of the streamwise mean velocity, i.e. $|\mathbf{U}|$ rather than the total velocity. The top boundary $(y = \delta)$ is taken to be a stress-free, slip surface. Periodic boundary conditions are applied in the streamwise and spanwise directions.

NUMERICAL APPROACH

Simulations are performed in a half channel configuration with domain extents $[L_x, L_y, L_z]/\delta = [2\pi, 1, 2\pi]$. The cross-plane grid resolution used for all simulations is $[N_y, N_z] = [144, 144]$. The non-zero streamwise wavenumber retained in the dynamics is $k_x \delta = 8$, and corresponds to a point in the outer-layer peak region of the vorticity spectra of an LES with equivalent grid resolution for a homogeneous rough wall configuration as detailed in Bretheim *et al.* (2018). Here the dimensional streamwise wavenumber is defined, $k_x = 2\pi n / L_x$ for some integer n.

We take advantage of the reduced number of streamwise wavenumbers in the RNL-LES dynamics by solving the governing equations in (k_x, y, z, t) space. This involves computing the components of the nonlinear terms involving streamwise interactions as a convolution instead of as a product in physical space, which reduces the need to apply transforms and saves computational time and resources, see Bretheim *et al.* (2018) for details.

The governing equations are solved in the pseudo-spectral code LESGO (https://lesgo.me.jhu.edu). Spectral derivatives are applied in the streamwise and spanwise directions, while second-order central finite differencing is used for wall-normal derivatives. The second-order explicit Adams-Bashforth method is used for time-marching. The 3/2-rule is used for dealiasing. The pressure Poisson equation is solved exactly by direct inversion in the streamwise and spanwise Fourier space, then discretizing the resulting ordinary differential equation using finite differencing in the wall-normal direction and applying the tri-diagonal matrix algorithm.

We consider a topography comprised of three repeating units, each of width $S = (2\pi/3)\delta$ and consisting of a high and low roughness strip. The topography is shown in the contour plot in Fig. 1, where black and white rectangles respectively indicate the high and low roughness regions. Within each unit the high roughness strip width is $\ell = 0.3125\ S$. This topography is imposed through an equilibrium wall-model where $y_{0,h} = 0.001\delta$ for the high roughness and $y_{0,l} = 0.01 y_{0,h}$ for the low roughness. This particular topography was selected because secondary flows have been reported to be dominant for the spacing $S \sim \delta$ (Wangsawijaya, 2020) and the particular roughness heights, $y_{0,h}$ and $y_{0,l}$, are similar to those used in other LES studies, e.g. Anderson (2015).

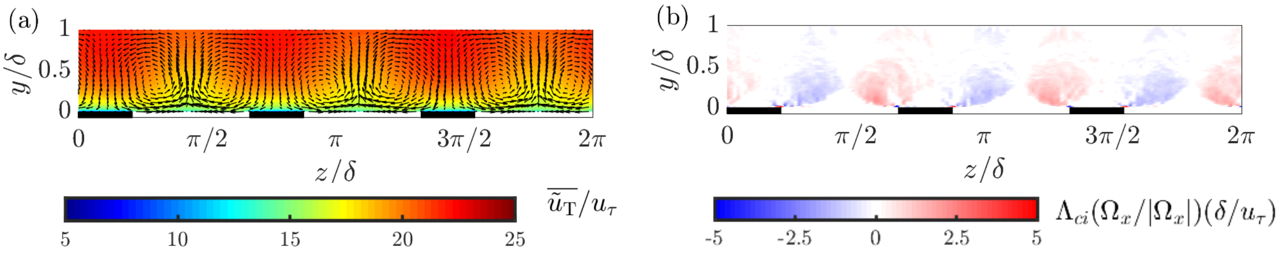

Figure 1: Time-averaged (a) velocity field and (b) swirl strength. The contour in (a) denotes the streamwise velocity field, arrows indicate the cross-plane velocity field and do not represent grid resolution.

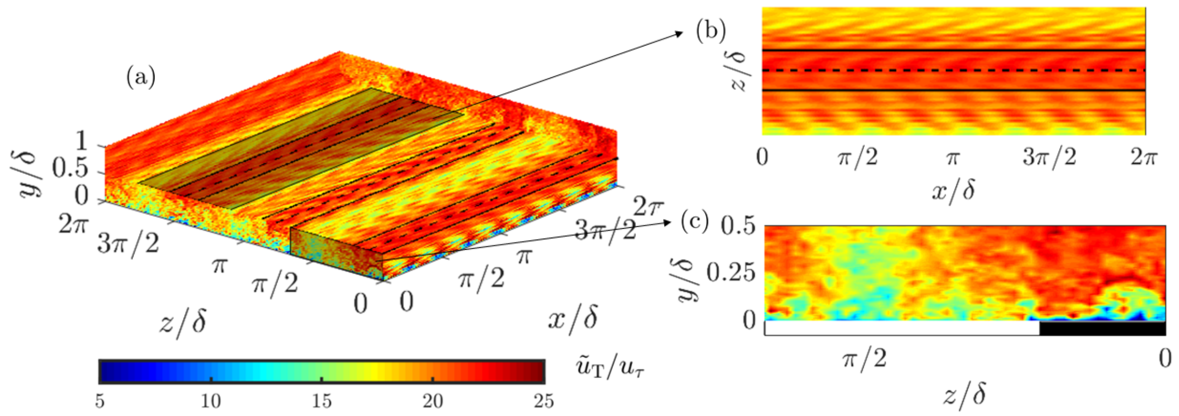

Figure 2: Instantaneous streamwise velocity field. Thick black lines in panel (a) show the borders of the high roughness regions centered at black dashed lines. Shaded regions in panel (a) are shown up close in panels (b) and (c). The xz-plane in (b) is taken at height $y = \delta/2$.

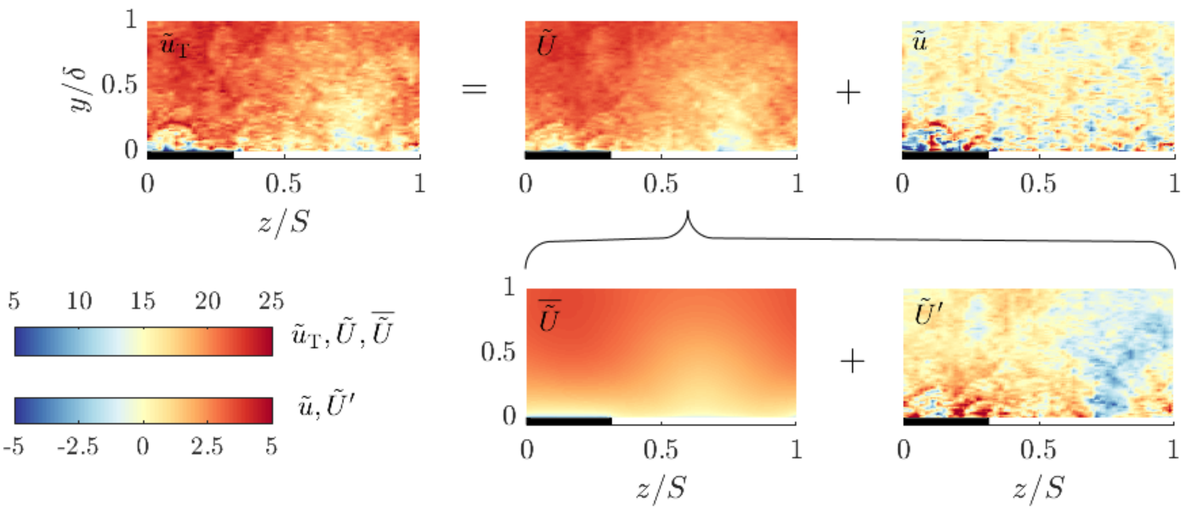

Figure 3: Instantaneous streamwise velocity field, $\tilde{u}_T$ decomposed into the streamwise averaged mean, $\tilde{U}$, and streamwise varying perturbation, $\tilde{u}$, components. The mean component is further decomposed into a time-average, $\overline{\tilde{U}}$, and fluctuation, $\tilde{U}'$, component. All quantities are non-dimensionalized by u_τ.

RESULTS

Fig. 1 demonstrates that the RNL-LES model is capable of reproducing time-averaged features of turbulent flow over spanwise heterogeneous roughness. The time-averaged streamwise velocity reported in Fig. 1a shows similar behavior to experimental and numerical studies, see e.g., Anderson (2015). Near the wall, lower streamwise velocity is observed over the high roughness region, which is a consequence of the boundary condition imposed. This trend changes far from the wall, where HMPs and LMPs are observed over the high and low roughness regions respectively. The formation of these pathways is highly dependent on the secondary flow, visualized by arrows in Fig. 1a. A pair of time-averaged streamwise rolls with alternating directions is observed for each high/low

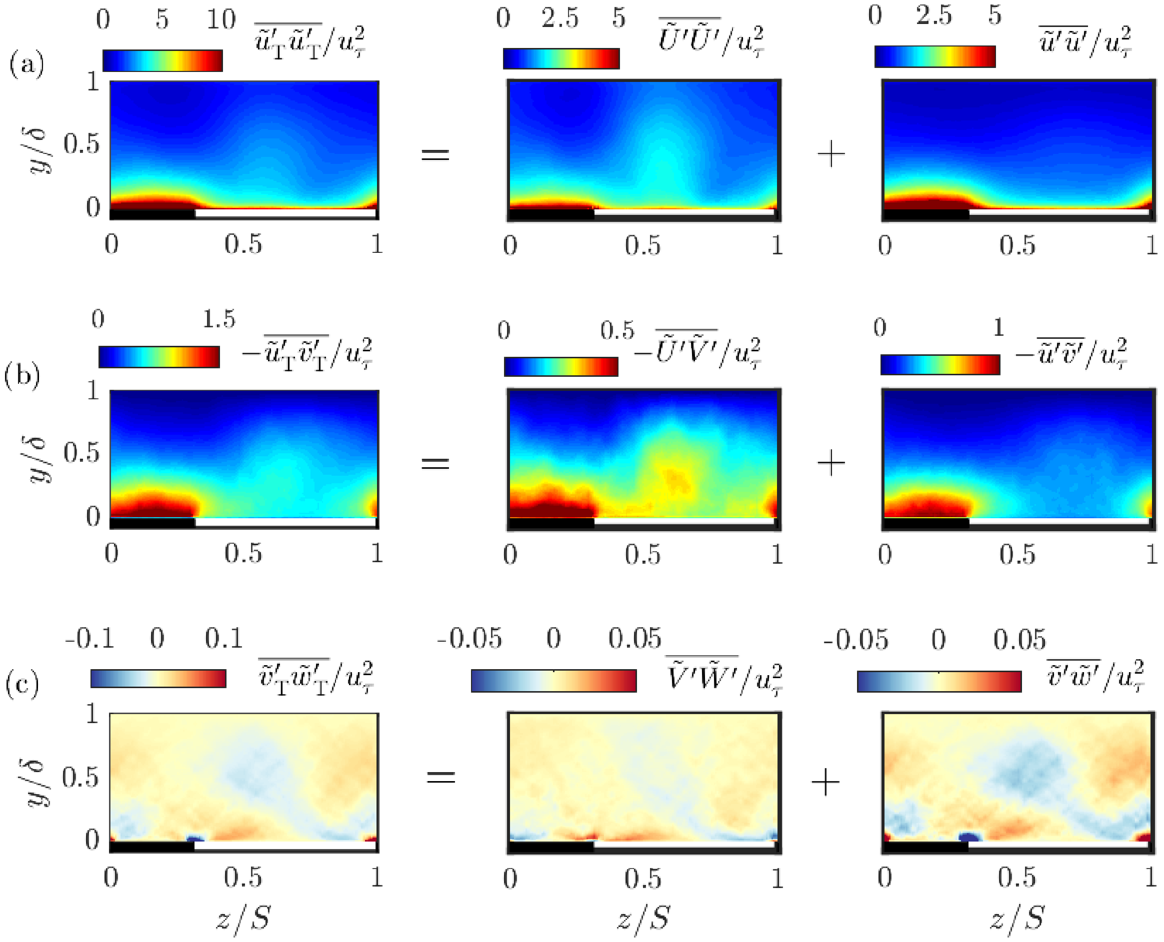

Figure 4: Total Reynolds stress decomposed into RNL-LES streamwise averaged mean (large-scale) and streamwise varying perturbation (small-scale) components. Results shown over one repeating roughness unit.

roughness region, centered at $y \approx \delta/2$. The location and orientation of this secondary flow is comparable to results reported in Anderson (2015), as is the intensity, visualized using the swirl strength in Fig. 1b. The ability of the RNL-LES model to accurately predict the time-averaged secondary flow and corresponding momentum pathways is a result of the streamwise constant nonlinearity retained in the model dynamics.

Fig. 2 shows a three dimensional perspective of an instantaneous snapshot of the streamwise velocity field at the mid-plane of the half-channel. Here the boundaries of the high roughness regions are indicated by solid black lines. At $y \approx \delta/2$ where the secondary flow is dominant, high and low speed streaks represented by the RNL mean are shown to align with high and low roughness regions respectively. Although these high and low speed large-scale structures are organized preferentially over the respective roughness regions, they meander instantaneously - a phenomenon introduced in Kevin (2017). Among these large-scale streaks, a single small-scale streamwise wavelength, represented by the perturbation component, is shown to be prevalent. This perturbation component, which is loosely coupled to the mean, is thought to reenergize the large-scale streaks. In the cross-plane, the sum of these components is shown to produce multi-scale behavior.

In Fig. 3 we show the RNL mean and perturbation components and how they contribute to the total streamwise velocity at a particular streamwise location and time instance. The cross plane snapshots indicate that, as expected, the streamwise average mean velocity acts as a large-scale in that it effectively filters small scale activity. The perturbation field is supported by a single streamwise wavenumber but full scale variation is observed in the cross plane. The intensity of the perturbation component is particularly high just over the high roughness strip. The RNL mean component is further decomposed into a time-average, $\overline{\tilde{U}}$, and fluctuation, $\tilde{U}'$, components in the bottom row of Fig. 3. Note that since time-averaged quantities are independent of streamwise location, $\overline{\tilde{u}_T} = \overline{\tilde{U}}$ and $\overline{\tilde{u}} = 0$. This decomposition reveals that while the time-fluctuating component of the streamwise average mean contributes to the total fluctuations, it comprises larger cross-plane scales than the perturbation component.

Having illustrated the characteristics of the RNL mean and perturbation components for a given instance, we next report the contributions of each towards various Reynolds stresses in Fig. 4. Since both the mean and perturbation components of the RNL model are time-fluctuating, they both contribute to the total Reynolds stress. Furthermore with only two streamwise wavenumbers, $k_x\delta = 0, 8$, simulated in the RNL-LES model these results are equivalent to modelled one-dimensional spectra varying in the spanwise and wall-normal directions. We therefore treat Reynolds stress involving the streamwise averaged mean as spectra from cumulative large-scales and Reynolds stresses involving streamwise perturba-

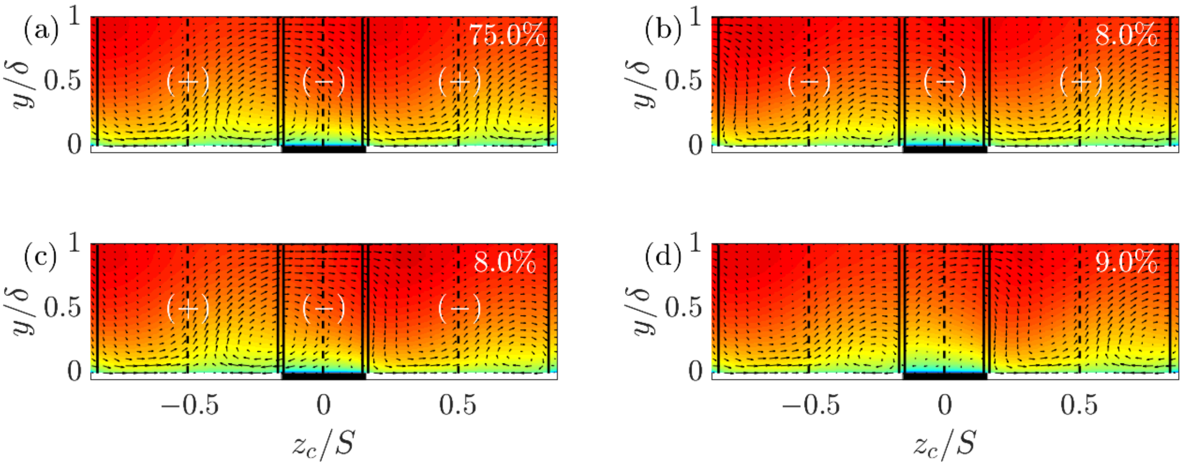

Figure 5: Conditionally averaged velocity fields based on direction of locally averaged wall-normal velocity performed over the entire high roughness region (indicated by black rectangle) and low roughness regions (centered by solid black line and bounded by dotted lines). Direction of flow in these regions indicated by +/- respectively denoting upwash/downwash. All five other possible combinations [(+,+,+),(+,+,-),(-,+,+),(-,+,-),(-,-,-)] not shown in panels (a-c) are included in (d). Color bar for streamwise velocity contour same as Fig. 2.

tions as spectra from small-scales.

The large-scale component of the streamwise Reynolds stress, $\overline{\tilde{U}'\tilde{U}'}$, shows higher energy in the outer-layer over the low roughness region near the center of the time-averaged secondary flow. This is consistent with observations in the experimental work of Wangsawijaya (2020), which suggests the secondary flow supplies additional energy to the very large-scale motions. The small-scale component, $\overline{\tilde{u}'\tilde{u}'}$, contributes little to this outer-layer energy, and only peaks near the wall particularly over the high roughness region. A similar trend is observed for the dominant Reynolds stress that acts in the streamwise momentum equation, $\overline{\tilde{u}'_T\tilde{v}'_T}$. Both the RNL mean and perturbation components contribute to this Reynolds stress and, as expected, the small-scale perturbations exchange momentum more in the near wall region and the large-scale mean exchanges momentum further from the wall. Similar to the streamwise Reynolds stress, a larger exchange of momentum is observed further from the wall over the low roughness strip, particularly in the mean component, indicating the large-scale secondary motions enhance mixing in this region.

The $\overline{\tilde{v}'_T\tilde{w}'_T}$ Reynolds stress is of significance as its gradients are responsible for the production of the secondary flow Anderson (2015). The RNL decomposition of this Reynolds stress reveals the small-scale component, $\overline{\tilde{v}'\tilde{w}'}$, is dominant, particularly near the wall at the roughness transition. The sharp sign change in this Reynolds stress at the roughness transition is not observed in the large-scale component, $\overline{\tilde{V}'\tilde{W}'}$, suggesting only small-scales play a role in the generation of secondary flow.

Isolating the large-scales of this flow into the streamwise average mean representation of the RNL decomposition enables structural features of the momentum pathways and secondary flow to be interrogated directly. We next exploit this structure in performing a conditional averaging analysis similar to that of Kevin (2017) to illustrate streak meandering and other features masked by time-averaging. Instantaneous flow samples are sorted according to the direction of the locally averaged wall-normal velocity of the large-scale streamwise mean centered over a high roughness region and the two neighboring low roughness regions. The spanwise boundaries in which these local averages are performed, are indicated by solid black lines in Fig. 5, with the center location indicated by the dashed black line. The local averages are performed over the entirety of the corresponding roughness region and the wall-normal direction. It should be noted that this analysis can be sensitive to the chosen width of the local averages, and the one chosen here is larger than the one used in Kevin (2017), however the overall trends illustrating the secondary flow direction and streak meandering will remain relatively unaffected.

Fig. 5 shows the results from this conditional averaging across a total of 70000 samples organized into four bins respectively shown in panels (a)– (d): bin 1 (+,-,+), bin 2 (-,-,+), bin 3 (+,-,-), and bin 4, which includes the other five combinations. Here the +/- sign is used to denote the upward/downward direction of the locally averaged wall-normal velocity of the streamwise averaged mean component in each region. The order of the combination denotes the location of each local average, from left to right: over the low roughness strip, the high roughness strip, then the other low roughness strip. Included in this figure is the percentage of samples used to develop each conditional average. Additionally, we denote the spanwise position in these figures as z_c, taking $z_c = 0$ to denote the center of the high roughness region and $z_c = \pm 0.5S$ as the center of the neighboring low roughness regions.

The case (+,-,+) which is most comparable to the time-average velocity field is shown to be predominant, more-so than the case considered in Kevin (2017), however this is likely due to the choice of conditional averaging width. Regardless, it is clear that a flow behavior different than the time-averaged sense occurs relatively often. Similar to the results in Kevin (2017), cases where downwash exists simultaneously over the high roughness region and a neighboring low roughness region, i.e., those denoted (-,-,+) and (+,-,-), occur often.

The downwash region of the (-,-,+) and (+,-,-) cases continue to show a time-averaged vortex, however reduced in size and magnitude. Interestingly, the streamwise momentum in this region is notably higher than the overall time-average field indicating a conditionally averaged high momentum pathway between the high and low roughness region coinciding with the conditionally averaged downwash. This behavior, well described within the RNL framework, is a result of the streamwise component of the mean equation, U responding to the secondary flow, (V,W), as a passive scalar only subject to small-scale forcing. In other words, streak meandering and secondary flow have a one-way coupling where the secondary flow drives streak meandering. This coupling is imposed in the RNL mean but given the similarity in behavior observed in experiments this type of coupling may persist in the full system.

CONCLUSION

An RNL-LES model is shown to reproduce the momentum pathways formed from secondary flow induced by spanwise heterogeneous strip roughness. The natural scale decomposition of this framework is then exploited to isolate the role of large and small streamwise scales in these secondary motions. An analysis of scale dependent streamwise Reynolds stress indicates that large-scale low speed streaks over the low roughness accumulate energy from the secondary flow. The small-scale component of the $\overline{\tilde{v}'_{\mathrm{T}}\tilde{w}'_{\mathrm{T}}}$ Reynolds stress is observed to be dominant near the wall at the roughness transition, suggesting small-scales are primarily responsible for the generation of the secondary flow.

Conditional averaging based on the direction of the wall-normal velocity of the RNL mean component over the low and high roughness regions is performed to quantify streak meandering. Upwash over low roughness regions and downwash over the high roughness region, as observed in the time-averaged flow field, is predominant however not the only instance observed. The other cases, that occur approximately a quarter of the time, show less intense secondary flow coinciding with an intensified streamwise momentum streak.

The RNL dynamics appears to provide a minimal representation of the streak-vortex instability model described in Jeong *et al.* (1997) and reasoned to be the mechanism for outer-layer streak meandering in spanwise heterogeneous roughness (Kevin *et al.*, 2019). The construction of the RNL model and its ability to reproduce this meandering suggests a one-way coupling wherein secondary flow leads to meandering. Further analysis of this interaction is a direction of ongoing work.

Another possibility for future study further investigation of the role of small-scales and their response to streak meandering. The RNL-LES model could prove useful for such a study as it readily represents smaller scales as a streamwise perturbation component. It may also prove insightful to investigate this meandering behavior for varying high roughness width to low roughness width ratio to further investigate the findings in Wangsawijaya (2020), where spanwise wavelength of the roughness was varied.

REFERENCES

Anderson, W., et al. 2015 Numerical and experimental study of mechanisms responsible for turbulent secondary flows in boundary layer flows over spanwise heterogeneous roughness. *J. Fluid Mech.* **768**, 316–347.

Awasthi, A. & Anderson, W. 2018 Numerical study of turbulent channel flow perturbed by spanwise topographic heterogeneity: Amplitude and frequency modulation within low- and high-momentum pathways. *Phys. Rev. Fluids* **3**, 044602.

Bai, Honglei, Kévin, Hutchins, Nicholas & Monty, Jason P. 2018 Turbulence modifications in a turbulent boundary layer over a rough wall with spanwise-alternating roughness strips. *Physics of Fluids* **30**, 055105.

Barros, J. M. & Christensen, K. T. 2014 Observations of turbulent secondary flows in a rough-wall boundary layer. *J. Fluid Mech.* **748**, R1.

Bretheim, J. U., Meneveau, C. & Gayme, D. F. 2018 A restricted nonlinear large eddy simulation model for high Reynolds number flows. *Journal of Turbulence* **19**, 141–166.

Chung, D., Monty, J. P. & Hutchins, N. 2018 Similarity and structure of wall turbulence with lateral wall shear stress variations. *J. Fluid Mech.* **847**, 591–613.

Farrell, B. F., Gayme, D. F. & Ioannou, P. J. 2017 A statistical state dynamics approach to wall turbulence. *Phil. Trans. R. Soc. A* **375**, 20160081.

Flack, K. A., Schultz, M. P. & Connelly, J. S. 2007 Examination of a critical roughness height for outer layer similarity. *Phys. Fluids* **19** (9), 095104.

Gayme, D. F. & Minnick, B. A. 2019 Coherent structure-based approach to modeling wall turbulence. *Phys. Rev. Fluids* **4**, 110505.

Hama, F.R., of Naval Architects, Society & Engineers, Marine 1954 *Boundary-layer Characteristics for Smooth and Rough Surfaces, by Francis R. Hama.*

Jeong, Jinhee, Hussain, Fazle, SCHOPPA , W. & Kim, John 1997 Coherent structure near the wall in a turbulent channel flow. *Journal of Fluid Mechanics* **332**, 185 – 214.

Kevin, Monty, J. P. & Hutchins, N. 2019 Turbulent structures in a statistically three-dimensional boundary layer. *J. Fluid Mech.* **859**, 543–565.

Kevin, et al. 2017 Cross-stream stereoscopic particle image velocimetry of a modified turbulent boundary layer over directional surface pattern. *J. Fluid Mech.* **813**, 412–435.

Minnick, Benjamin A. & Gayme, Dennice F. 2019 Characterizing energy transfer in restricted nonlinear wall-bounded turbulence. In *International Symposium on Turbulence and Shear Flow Phenomena (TSFP-11)*.

Moody, L.F. 1944 Friction factors for pipe flow. *Trans. ASME* **66** (8), 671–677.

Nikuradse, J. & Nikuradse, J. 1933 Laws of flow in rough pipes. *VDI Forschungsheft* p. 361.

Prandtl, L. 1952 *Essentials of Fluid Dynamics*. Hafner Publishing Company.

Schultz, M. P. & Flack, K. A. 2005 Outer layer similarity in fully rough turbulent boundary layers. *Exp. Fluids* **38** (3), 328–340.

Smagorinsky, J. 1963 General circulation experiments with the primitive equations: I. the basic experiment. *Monthly Weather Review* **91** (3), 99 – 164.

Thomas, V. L., Lieu, B. K., Jovanović, M. R., Farrell, B. F., Ioannou, P. J. & Gayme, D. F. 2014 Self-sustaining turbulence in a restricted nonlinear model of plane couette flow. *Phys. Fluids* **26** (10), 105112.

Townsend, A. A. R. 1980 *The structure of turbulent shear flow*. Cambridge university press.

Wangsawijaya, D. D., et al. 2020 The effect of spanwise wavelength of surface heterogeneity on turbulent secondary flows. *J. Fluid Mech.* **894**, A7.

Willingham, David, Anderson, William, Christensen, Kenneth T & Barros, Julio M 2014 Turbulent boundary layer flow over transverse aerodynamic roughness transitions: induced mixing and flow characterization. *Physics of Fluids* **26** (2), 025111.